AGU PUBLICATIONS

JGR

Journal of Geophysical Research: Space Physics

RESEARCH ARTICLE
10.1002/2016JA022489

Key Points:
- Simultaneous presence of positive and negative storms in American sector
- Equatorward shift and enhancement of the midlatitude density trough in the American longitude sector
- Strong hemispheric asymmetry in the negative storm phase during recovery phase

Correspondence to:
C. Nayak,
physics642@gmail.com

Citation:
Nayak, C., L.-C. Tsai, S.-Y. Su, I. A. Galkin, A. T. K. Tan, E. Nofri, and P. Jamjareegulgarn (2016), Peculiar features of the low-latitude and midlatitude ionospheric response to the St. Patrick's Day geomagnetic storm of 17 March 2015, *J. Geophys. Res. Space Physics*, *121*, 7941–7960, doi:10.1002/2016JA022489.

Received 5 FEB 2016
Accepted 21 JUL 2016
Accepted article online 25 JUL 2016
Published online 9 AUG 2016

Peculiar features of the low-latitude and midlatitude ionospheric response to the St. Patrick's Day geomagnetic storm of 17 March 2015

Chinmaya Nayak[1], L.-C. Tsai[1], S.-Y. Su[1], I. A. Galkin[2], Adrian Teck Keng Tan[3], Ed Nofri[4], and Punyawi Jamjareegulgarn[5]

[1]Center for Space and Remote Sensing Research, National Central University, Taoyuan, Taiwan, [2]Center for Atmospheric Research, University of Massachusetts Lowell, Lowell, Massachusetts, USA, [3]DSO National Laboratories, Singapore, Singapore, [4]National Institute of Aeronautics and Space (LAPAN), Jakarta, Indonesia, [5]Department of Engineering, King Mongkut's Institute of Technology Ladkrabang, Chumphon, Thailand

Abstract The current study aims at investigating and identifying the ionospheric effects of the geomagnetic storm that occurred during 17–19 March 2015. Incidentally, with *SYM-H* hitting a minimum of −232 nT, this was the strongest storm of the current solar cycle 24. The study investigates how the storm has affected the equatorial, low-latitude, and midlatitude ionosphere in the American and the European sectors using available ground-based ionosonde and GPS TEC (total electron content) data. The possible effects of prompt electric field penetration is observed in both sectors during the main phase of the storm. In the American sector, the coexistence of both positive and negative ionospheric storm phases are observed at low latitudes and midlatitudes to high latitudes, respectively. The positive storm phase is mainly due to the prompt penetration electric fields. The negative storm phase in the midlatitude region is a combined effect of disturbance dynamo electric fields, the equatorward shift of the midlatitude density trough, and the equatorward compression of the plasmapause in combination with chemical compositional changes. Strong negative ionospheric storm phase is observed in both ionosonde and TEC observations during the recovery phase which also shows a strong hemispherical asymmetry. Additionally, the variation of equatorial ionization anomaly as seen through the SWARM constellation plasma measurements across different longitudes has been discussed. We, also, take a look at the performance of the IRI Real-Time Assimilative Mapping during this storm as an ionospheric space weather tool.

1. Introduction

The effect of geomagnetic disturbance on the Earth's ionosphere has been studied extensively not only for scientific interests [*Prolss*, 1978; *Yeh et al.*, 1991; *Pavlov*, 1994; *Fejer and Scherliess*, 1995, 1997; *Sastri et al.*, 2000; *Basu et al.*, 2001; *Richards and Wilkinson*, 1998; *Foster and Rich*, 1998; *Heelis et al.*, 2009] but also for practical purposes due to its ability to affect various branches of telecommunication and navigation [*Bhattacharyya et al.*, 2002; *Jakowski et al.*, 2005; *Basu et al.*, 2008; *Astafyeva et al.*, 2014]. The geomagnetic storm is a very complex process which starts as a sudden compression of the Earth's magnetosphere and the corresponding intensification of the ring current which is reflected in the *Dst* index. During the geomagnetic disturbance, energy and momentum input to the high-latitude upper atmosphere is suddenly increased. Due to the resultant Joule heating, it gets heated up and starts expanding, giving rise to winds, equatorward surges, traveling atmospheric disturbances, and changes in thermospheric composition [*Prolss*, 1978]. The storm time disturbances can affect and substantially modify the ambient ionospheric electric fields at equatorial, low, middle, and high latitudes, due to either prompt penetration of the electric field of magnetospheric origin [*Nishida*, 1968; *Spiro et al.*, 1988; *Kikuchi et al.*, 1978, 2008] or the disturbance dynamo (DD) [*Blanc and Richmond*, 1980] or a combination of both [*Maruyama et al.*, 2005; *Kakad et al.*, 2007]. In terms of ionospheric electron density, the ionospheric storms are generally divided into two categories. The storms associated with enhancement in electron density are termed as positive ionospheric storms, whereas those associated with decrease in electron density are termed as negative ionospheric storms. Whereas the negative storm phases are mainly associated with compositional changes [*Proelss*, 1987], the positive storm phases can be caused by compositional changes [*Fuller-Rowell et al.*, 1996], by transport of ionization or electric field changes, or by thermospheric winds [*Prölss et al.*, 1991; *Prölss*, 1993; *Reddy*, 1992].

Table 1. Details of Ionosonde Stations

Station Code	Station Name	Geographic Latitude (deg)	Geographic Longitude (deg)	Magnetic Dip (deg)
bldr	Boulder, USA	40.0	−105.3	66.52
bvst	Boa Vista, Brazil	2.80	−60.70	18.78
egln	Eglin, USA	30.50	−86.50	59.85
jmrc	Jicamarca, Peru	−12.00	−76.8	0.04
mlst	Milstone Hill, USA	42.6	−71.56	7.57
rame	Ramey, Puerto Rico	18.50	−67.10	44.15
athn	Athens, Greece	38.0	23.5	54.56
grst	Grahamstown, South Africa	−33.3	26.5	−64.10
hrmn	Hermanus, South Africa	−34.42	19.22	−65.76
juli	Juliushru, Germany	54.6	13.4	69.35
lous	Louisevale, South Africa	−28.5	21.2	−65.69
snvt	San Vito, Italy	40.6	17.8	57.08

The geomagnetic storm of 17 March 2015, also termed as the St. Patrick's Day storm, is special in the sense that it was the strongest geomagnetic storm observed till now during the current solar cycle 24. It must be noted that the background ionospheric conditions were much different during the extended solar minimum period of solar cycle 24 as compared to the previous solar minimum [*Solomon et al.*, 2013; *Liu et al.*, 2011, 2012]. At the same time the maximum phase of the current solar cycle does not seem as strong as the last one. Hence, it was worthy to investigate various ionospheric effects the St. Patrick's Day storm had on the Earth's ionosphere. Being the strongest geomagnetic storm of the current solar cycle, this particular event has garnered considerable interest in the scientific community. *Astafyeva et al.* [2015] reported the ionospheric effects of the storm on a global scale. *Liu et al.* [2016] has studied the storm-enhanced density during the main phase of the storm. The studies by *Ram et al.* [2015] and *Ramsingh et al.* [2015] mostly concentrated on the ionospheric effects observed near the equatorial latitudes of the Indian and nearby regions. In the present study, we have mainly focused on the ionospheric variations in the low-latitude and midlatitude regions along with the underlying physical mechanisms as seen in two different longitudinal sectors, namely, the American and the European sectors.

2. Data Used

To have a complete picture of spatiotemporal variation of the ionosphere during the geomagnetically disturbed conditions, both ground-based and in situ satellite measurements have been utilized in the study.

2.1. Ground-Based Ionograms and GPS TEC

Since we are looking to investigate the global ionospheric response, we have selected a latitudinal chain of ionosonde (digisonde) stations each, across two different longitudinal sectors to have a better picture of both latitudinal and longitudinal pictures. The coordinates of the ionosonde stations have been listed in tabular form and shown in Table 1. The digisonde data have been downloaded and analyzed using the SAO Explorer which can be obtained from http://ulcar.uml.edu/SAO-X/SAO-X.html. SAO stands for standard archival output, the abbreviation used for the ionogram-derived data. Further details about the SAO Explorer can be obtained from *Khmyrov et al.* [2007].

We have also used the ground-based GPS (Global Positioning System) total electron content (TEC) data obtained from the SOPAC (Scripps Orbit and Permanent Array Center) data browser which can be reached at http://sopac.ucsd.edu/dataBrowser.shtml. The names and coordinates of the ground GPS TEC stations have been tabulated and shown in Table 2. Figure 1 shows the exact locations of the ionosonde stations (marked by black squares) and the IGS (International GNSS (Global Navigation Satellite Systems) Service) GPS stations (marked by red circles) employed for this study.

2.2. SWARM

SWARM is a recent mission of the European Space Agency (ESA) which was launched with the aim of studying the dynamics of the Earth's magnetic field and its interactions with the Earth system. It consists of a constellation of three satellites (A, Alpha; B, Bravo; and C, Charlie). Satellites A and C fly at an altitude of 460 km with

Table 2. Details of GPS Stations

IGS Code	Station Name	Geographic Latitude (deg)	Geographic Longitude (deg)	Magnetic Dip (deg)
adis	Adis Ababa, Ethiopia	9.03	38.76	2.27
ankr	Ankara, Turkey	39.88	32.75	57.67
antc	Los Angeles, Chile	−37.33	−71.53	−37.97
arev	Arequipa, Peru	−16.46	−71.49	−8.92
bogt	Bogota, Colombia	4.64	−74.08	28.54
bshm	Haifa, Israel	32.77	35.02	49.08
cags	Gatineau, Canada	45.58	−75.80	70.73
cord	Cordoba, Argentina	−31.52	−64.47	−33.39
crao	Simeiz, Ukraine	44.41	33.99	62.34
cro1	Christiansted, USA	17.75	−64.58	42.19
dear	De Aar, South Africa	−30.66	23.99	−65.04
falk	Port Stanley,Falkland/Malvinas Islands	−51.69	−57.87	−49.82
glsv	Kiev, Ukraine	50.36	30.49	67.14
hnpt	Cambridge, USA	38.58	−76.13	65.46
kuuj	Kuujjuarapik, Canada	55.27	−77.74	77.51
mbar	Mbarara, Uganda	−0.60	30.73	−24.68
mfkg	Mafikeng, South Africa	−25.80	25.53	−63.7
mgue	Malargue, Argentina	−35.77	−69.39	−36.65
mikl	Mykolaiv, Ukraine	46.97	31.97	64.48
nico	Nicosia, Cyprus	35.14	33.39	52.07
nurk	Kigali, Rwanda	−1.94	30.08	−28.05
ohi3	O,Higgins, Antartica	−63.32	−57.90	−56.28
parc	Punta Arenas, Chile	−53.13	−70.87	−49.74
ramo	Mitze Ramon, Israel	30.59	34.76	45.86
rbay	Richardsbay, South Africa	−28.79	32.07	−62.47
riop	Riobamba, Ecuador	−1.65	−78.65	19.01
sch2	Schefferville, Canada	54.83	−66.83	75.36
sutm	Sutherland, South Africa	−32.38	20.81	−65.77
svtl	Svetloe, Russian Federation	60.53	29.78	73.85
tdou	Thohoyandou, South Africa	−23.07	30.38	−60.65
unsa	Salta, Argentina	−24.72	−65.40	−24.48
vald	Val DOr, Canada	48.09	−77.56	72.8

a 1–2° of separation in longitude. Satellite B flies at an approximate altitude of 540 km. Although the main aim of the SWARM mission is to provide magnetic field data, it also gives the in situ measurements of the electron density (Ne) obtained from the Langmuir Probe on board the individual SWARM satellites. In this study, we have used this in situ electron density (Ne) data to investigate the structure of the equatorial ionization anomaly (EIA). Since all the satellites fly close by, and the data from the other two satellites also show similar results, we confined our attention to data from SWARM A only. Also, we have considered only the postsunset crossings of SWARM A which has an equatorial crossing of approximately 20 LT. Since the orbital inclination of the satellite is 87.5°, the local time remains almost the same across most of the latitudes in each crossing.

2.3. International Reference Ionosphere Real-Time Assimilative Mapping Global Maps

To have a global overview of the ionospheric conditions during the storm time, we have used the global f_oF_2 maps produced by the International Reference Ionosphere (IRI) Real-Time Assimilative Mapping (IRTAM) model. The IRTAM is capable of producing near-real-time global maps of f_oF_2 and h_mF_2 using measured data from around 70 ionosonde stations of the Global Ionosphere Radio Observatory (GIRO) [*Reinisch and Galkin*, 2011], usually at a 15 min resolution. The IRTAM uses the International Reference Ionosphere (IRI) electron density model [*Bilitza et al.*, 2011] as the background model. The IRI model uses the so-called CCIR (Comite Consultatif International des Radiocommunications) or URSI (International Union of Radio Science) coefficients

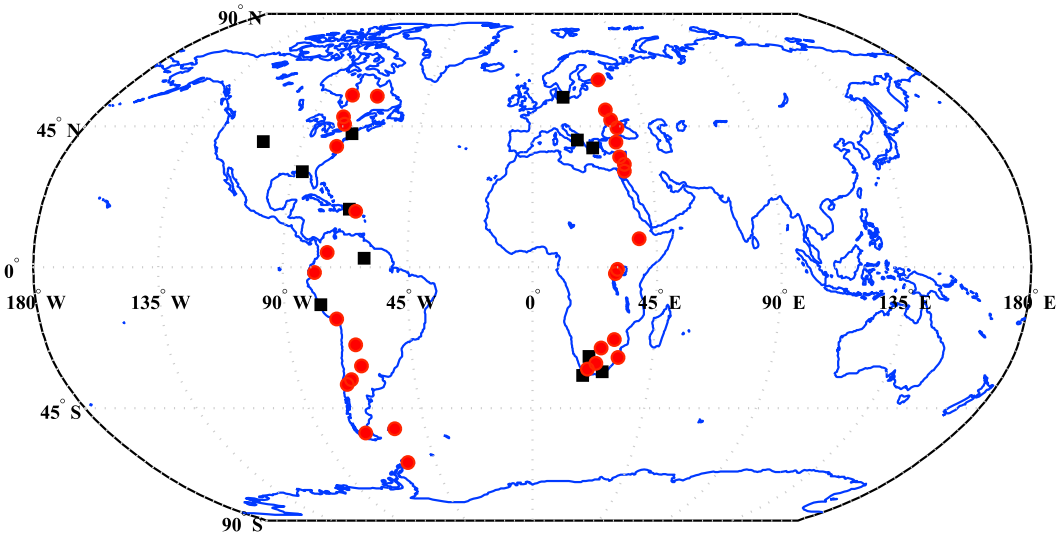

Figure 1. Locations of ionosonde and GPS TEC stations. The black squares represent the ionosonde stations, whereas the red circles represent the IGS GPS TEC stations.

for the specification of the median f_oF_2 and h_mF_2 maps. IRTAM assimilates the measured GIRO data in IRI by adjusting the CCIR coefficients on the fly. Further details about the IRTAM can be obtained from *Galkin et al.* [2012].

2.4. TIMED-GUVI Global O/N_2 Ratio Maps

To have a rough idea of the varying thermospheric neutral density, we have utilized the thermospheric O/N_2 global maps obtained from Global Ultraviolet Imager (GUVI) instrument on board TIMED (Thermosphere Ionosphere Mesosphere Energetics and Dynamics) spacecraft. It gives the thermospheric column number density ratio of O and N_2 referenced at N_2 column number density level of 10^{17} cm^{-2}. The procedure to produce the global O/N_2 maps can be found at http://guvi.jhuapl.edu/site/data/documents/on2_info.html. The global maps themselves can be obtained from http://guvi.jhuapl.edu/site/gallery/guvi-galleryl3on2.shtml.

3. The Storm

On 15 March 2015, a magnetic filament eruption from sunspot no 2297 led to a partial halo coronal mass ejection (CME) with an Earth-directed component. A few hours later, the Earth's magnetosphere was hit by the CME at around 04:30 UT and a series of events led to the evolution of the strongest geomagnetic storm of solar cycle 24. The solar wind plasma and magnetic parameters at Earth's bow shock nose have been shown in Figure 2. These data have been obtained from NASA's Space Physics Data Facility's OMNIweb data explorer (http://omniweb.gsfc.nasa.gov) which combines the measurements from WIND and ACE spacecrafts to provide us the time series data. The advent of the CME can be seen as a sudden increase in solar wind pressure (Figure 2a), flow speed (Figure 2b), and the interplanetary magnetic field (IMF) (Figure 2c) at around 04:45 UT. In turn, the *z* component of the interplanetary magnetic field (IMF B_z) (Figure 2d) becomes strongly northward and the symmetrical ring current index *SYM-H* (Figure 2f) is suddenly enhanced representing the sudden storm commencement. The corresponding variations in the interplanetary electric field is shown in Figure 2e. Subsequently, the IMF B_z turns southward at 06:00 UT. Although the IMF B_z recovers for some hours initially, it turns southward again approximately for the next 12 h before recovering. During this period the *SYM-H* drops to a minimum of −233 nT at 22:45 UT, signifying the strongest storm of this solar cycle, in terms of magnitude. For our convenience, let us divide the storm into two parts. The first part may be considered from 04:45 UT to 12:00 UT on 17 March 2015, during which the IMF B_z turns southward for the first time and *SYM-H* reaches a minimum of around 110 nT before registering a slight recovery with northward turning IMF B_z. The second part may be considered as the rest of the storm after 12:00 UT during which IMF B_z turns and stays southward for approximately 12 h and *SYM-H* reaches the minimum of −232 nT before starting the recovery phase. As shown in Figure 2, the time of sudden commencement is marked by the vertical red dotted line (4.65 UT, 17 March 2015), whereas the time of first minimum in *SYM-H* is marked with the vertical green dotted lines

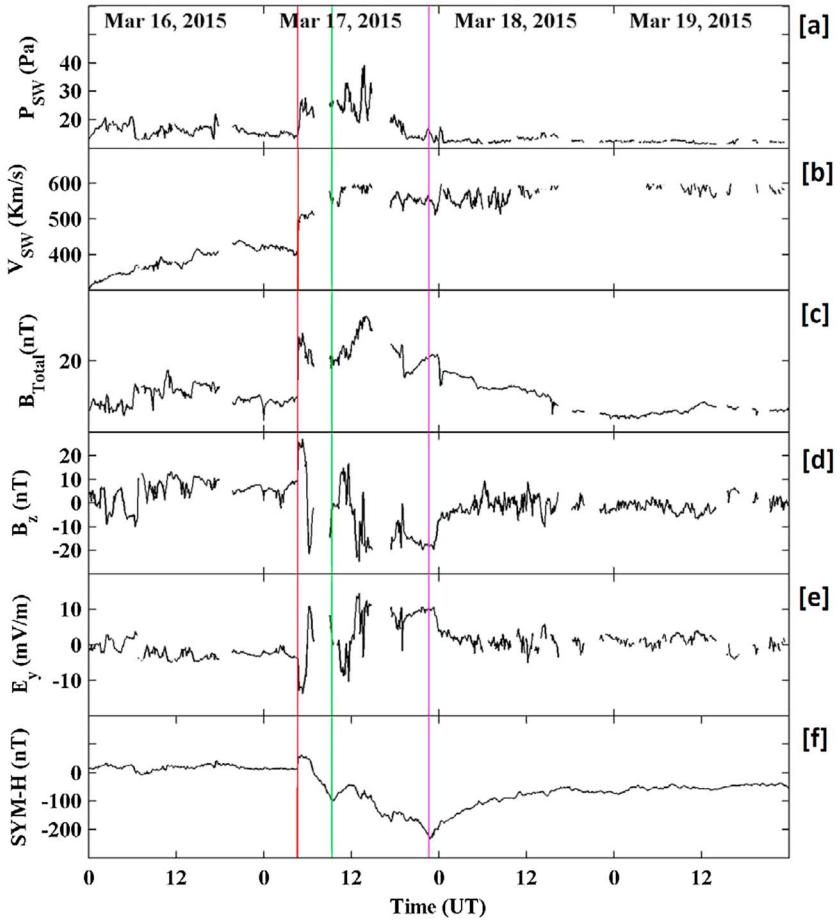

Figure 2. Geomagnetic conditions during 16–19 March 2015. The red vertical line represents the time of sudden storm commencement. The green line represents the time when *SYM-H* reached a first minimum before registering a slight recovery. The magenta line represents the time when *SYM-H* reached its actual minimum of −232 nT which signifies the maximum phase of the storm. The same notations are used in other figures as well, throughout the paper.

(9.4 UT, 17 March 2015). The time of actual minimum (−232 nT at 22:45 UT) is marked with vertical magenta dotted lines (22.7 UT, 17 March 2015).

As per the current understanding, when the IMF B_z turns southward, due to enhanced convection electric field, eastward prompt penetration electric fields (PPEF) are observed in the dayside ionosphere and corresponding westward PPEF are observed in the nightside ionosphere [*Nishida*, 1968; *Kikuchi et al.*, 1996, 2000]. It should be noted that in this case (southward turning of IMF), the PPEF are in the directions the same as that of the global dawn-dusk equatorial zonal electric field. However, during sudden northward turning of the IMF B_z, the PPEFs that penetrate to equatorial and low-latitude ionosphere are generally in the directions opposite to those of the dawn-dusk zonal electric fields [*Kelley et al.*, 2003]. In simple words, PPEFs during southward turning of IMF B_z can strengthen the existing ionospheric zonal electric fields, whereas during northward turning of IMF B_z, the PPEFs can weaken the existing zonal electric fields. So in our case, most of the PPEF effects are expected to be observed around a few hours on both sides of the green vertical line during which most of the IMF B_z turning takes place.

4. Results and Discussion

Figure 3 represents the ionospheric variability as seen through ionograms, during 17–19 March 2015 in the American sector. Figures 3a–3f represent the variations in critical frequency (f_oF_2) of the ionospheric F_2 layer, whereas Figures 3g–3l represent the variations in the height of the maximum electron density (h_mF_2). The black curve represents the mean quiet day pattern with the error bars represented in green. The mean quiet day patterns are calculated using the data for the five quietest days of the month (5, 9, 10, 14, and 15 March).

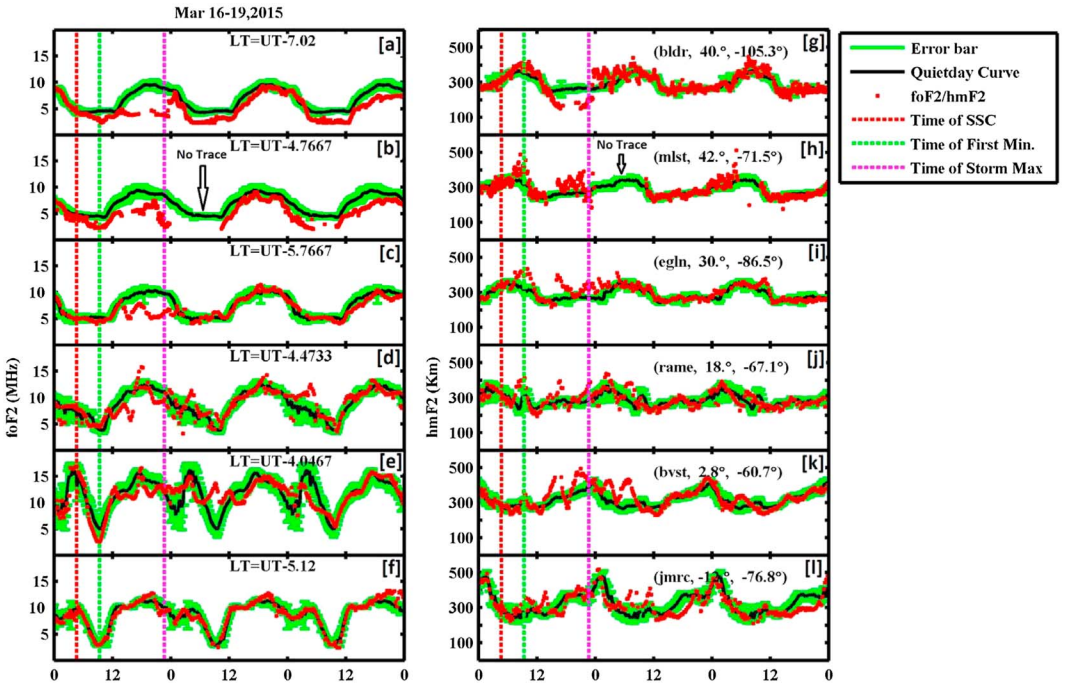

Figure 3. Variations of ionospheric parameters in the American sector. (a–f) The variations in f_oF_2 and (g–l) the variations in h_mF_2. The black solid lines with green error bars represent the quiet time pattern. The red dots represent the storm time parameter (f_oF_2 for Figures 3a–3f and h_mF_2 for Figures 3g–3l).

The red curves represent the ionospheric parameters during 17–19 March 2015. For Figures 3a–3f, the red curves represent the variations in f_oF_2. Similarly, in Figures 3g–3l, the variations of h_mF_2 are shown in red. Similar notations are used in Figure 4 for the European sector.

It should be noted that out of the six stations mentioned in Figure 3, Jicamarca is an equatorial (geomagnetic) station, whereas others are low-latitude and midlatitude stations located in the Northern Hemisphere. Unfortunately, we could not find data from a station in the Southern Hemisphere. For the European sector, out of six stations, three are midlatitude stations from the Northern Hemisphere, whereas the other three are midlatitude stations in the Southern Hemisphere. No equatorial ionosonde station's data were available in the European sector.

Looking at the h_mF_2 variations in the American sector (Figures 3g–3l), it can be seen that there is no noticeable effect at the time of sudden commencement. The first significant effect can be seen around the green dotted line which represents the first minimum of the *SYM-H*. It is easy to notice that there is an enhancement in h_mF_2 at all stations. The enhancement seems smaller at the equatorial station Jicamarca but relatively higher at the other stations except Boulder station. The same enhancement in h_mF_2 can also be seen in the European sector (Figures 4g–4l). Though this enhancement is not very clear in the Southern Hemisphere, it can be seen in the northern one. This can be attributed to the prompt penetration electric fields associated with the fluctuating IMF B_z at that time. Although it is possible that the disturbance dynamo electric fields (DDEF) might have been set up by this time in the higher latitudes, it may not have reached the equatorial and low-latitude stations by this time. Also, the enhancement in h_mF_2 is seen across all stations for small duration (1–2 h). In case of DD electric fields, the effects could have been for longer durations. So we may attribute this to prompt penetration electric fields (PPEFs). In terms of f_oF_2, it shows a very small decrease in f_oF_2 across all stations in the American sector. On the other hand, the European sector shows slight increase in f_oF_2 for all stations at around 12 UT, just after the green vertical line.

4.1. Probable Presence of Simultaneous Positive and Negative Ionospheric Storm Phases?

Shortly after this point, around 12:00 UT, the IMF B_z starts turning southward and stays southward for approximately 12 h and *SYM-H* dips further reaching a minimum of 232 nT at around 22:45 UT (represented by the vertical magenta line). During this interval of time, a lot of changes take place across all stations in both sectors. In the American sector, except for Boulder and Milstone Hill, all other stations show an increase in h_mF_2

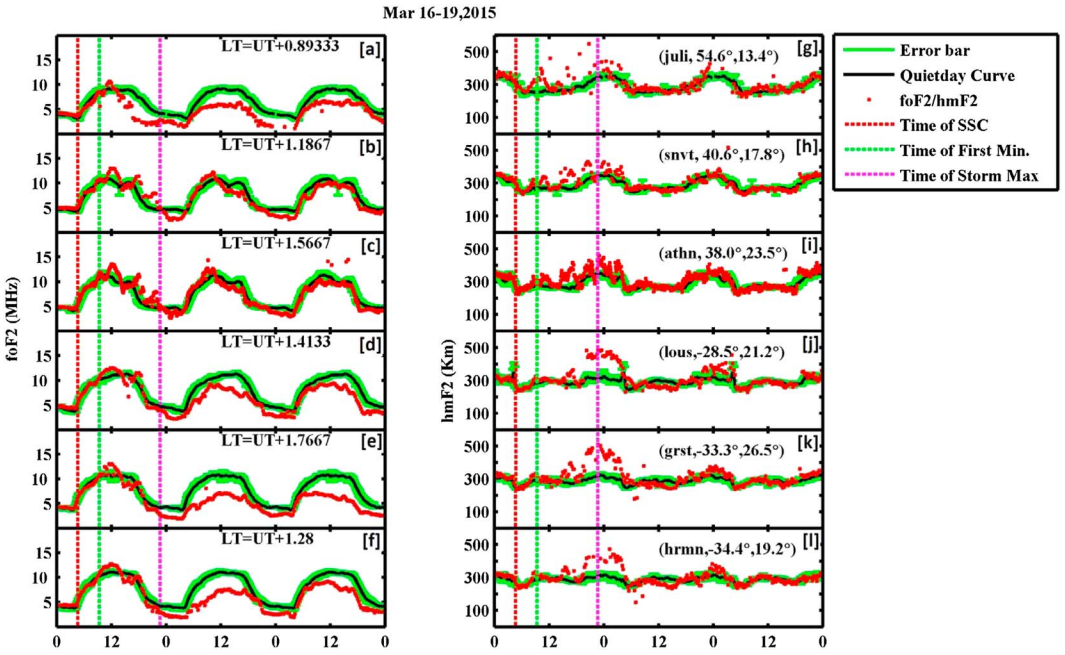

Figure 4. Variations of ionospheric parameters in the European Sector. (a–f) The variations in f_oF_2 and (g–l) the variations in h_mF_2. The black solid lines with green error bars represent the quiet time pattern. The red dots represent the storm time parameter (f_oF_2 for Figures 4a–4f and h_mF_2 for Figures 4g–4l).

followed by a decrease. More or less, the increased h_mF_2 shows an oscillating behavior at these stations. In case of Boulder (Figure 3g), we can see a clear and significant decrease in h_mF_2 indicating a downward moving ionosphere. In terms of f_oF_2, Boulder (Figure 3a), Millstone Hill (Figure 3b), and Eglin (Figure 3c) all show strong depletion in f_oF_2, whereas other stations do not show such strong decrease in f_oF_2. This may be an indication of development of the ionospheric disturbance dynamo. The decrease in h_mF_2 and f_oF_2 at Boulder starts around 12 UT. Since nearly 6 h have already passed from the storm onset, there is a fair possibility that the processes related to the ionospheric disturbance dynamo have already started, which are reflected in both h_mF_2 and f_oF_2 at Boulder. As we observe a downward drift of the ionosphere, in this case, the presence of a westward electric field, created due to the disturbance dynamo, cannot be neglected. However, it must be considered that the geomagnetic field lines are highly inclined at the location of Boulder. So the corresponding $E \times B$ drift alone may not have a vertical component strong enough to create such a strong downward drift of the ionosphere. So the westward electric field cannot be the sole driver for such a drastic change in both f_oF_2 and h_mF_2. We believe that another important factor in this case must be the changing thermospheric winds associated with the disturbance dynamo which contributes toward a faster recombination at those altitudes leading to the sharp decrease in f_oF_2 (electron density) and corresponding drop in h_mF_2. The disturbance dynamo effects are also seen at Eglin, although the effects are slightly less compared to those at Boulder and Millstone Hill. The rest of the stations do not show any such effects. This duration of time (between the green and the magenta vertical lines) is the period when we can see distinct effects of disturbance dynamo and prompt penetration electric fields at different latitudes. The disturbance dynamo effects have possibly reached up to the latitude of Eglin (30.5°N), whereas other stations (Ramey, Boa Vista, and Jicamarca) are yet to be touched by it and still under the effects of prompt penetration electric fields. However, as time progresses, the disturbance dynamo will gradually propagate and reach the equatorial and low-latitude stations.

If we look at the European sector (Figure 4), it is actually difficult to separate any PPEF and disturbance dynamo effects. Overall, all the stations in both hemispheres show an increase in h_mF_2 values (Figures 4g–4l). The biggest increase in h_mF_2 is recorded around the time when the *SYM-H* is at its minimum (represented by the vertical magenta line). The increase in h_mF_2 starts around 18:30 UT on 17 March 2015, and it stays well above the quiet day curve (represented by the black curve with green error bars) till 04:30 UT of the next day, i.e., 18 March 2015. So for almost 10 h, the ionosphere in the European sector is observed to be well above its normal range of altitude. For most part of this period, the IMF B_z is southward before turning northward eventually at around 00:00 UT of 18 March 2015. A closer look suggests that the effect is more prominent in the Southern

Hemisphere as compared to the northern one. If we look at the variation of f_oF_2, it can be seen that f_oF_2 decreases significantly at all the stations where we see the increase in h_mF_2. This depletion in plasma density may be caused by the advection of the nighttime plasma toward west as suggested by *Vlasov et al.* [2003]. During the process of advection, the nighttime plasma is dumped in the westward dayside sector causing the flux tubes in the nighttime sector to be emptied. So after the initial increase in f_oF_2 around 12 LT of 17 March 2015, the f_oF_2 gradually starts decreasing and becomes lower than its quiet day values for all stations as shown in Figures 4a–4f showing a negative ionospheric storm.

After 00UT on 18 March 2015, the IMF B_z gradually attains its quiet time values around 0 nT without much strong variations. So we do not expect much prompt penetration electric fields after this duration. Whatever effects of the prompt penetration electric fields may remain, they are supposed to die down in a couple of hours. So after 04:00 UT on 18 March 2015, the ionospheric dynamics is expected to be controlled by the disturbance dynamo. However, the period before this is a period where it is difficult to differentiate between the effects of prompt penetration and disturbance dynamo electric fields. At the same time, the PPEFs are generally short lived and incapable of acting for 10 h. So the almost 10 h rise in h_mF_2 may be due to the action of either a combined disturbance dynamo and prompt penetration (DDEF+PPEF) or only DDEF. However, it is impossible to reach a conclusion with the current observations.

A similar picture can also be inferred from Figure 5. Figure 5 shows the plot of ΔTEC (difference of storm time TEC − quiet time TEC) during 17–19 March 2015, for various stations in both sectors. The details of the stations have been shown in Table 2. Figure 5 (rows 1–16) represents ΔTEC in the American sector, whereas Figure 5 (rows 17–32) represents the stations in the European sector.

Coming back to 17 March 2015, for the American sector, at around 18:30 UT, a clear enhancement can be seen in TEC which is seen across all stations below 20°N latitude (Figure 5, rows 6–16). However, the stations above 38°N (Figure 5, rows 1–5) show a decrease in TEC values at the same time. This again proves the simultaneous presence of positive and negative ionospheric storm phases in the American sector, in different latitudes of the midlatitude regions. One possible reason for this may be that the changing thermospheric winds and the associated disturbance dynamo electric field (westward in this case) has reached up to 40°N by this time in the American sector. At the same time, below 40°N, the prompt penetration electric field is still active. That is why we are able to to see the coexistent positive and negative storm phases in the American sector. The probable simultaneous presence of the two storm phases can be seen up to 02:00 UT of 18 March 2015. The European sector, however, does not show any such coexistent storm phases. The disturbance dynamo-related effects are still above 60°N, which is why we do not see a negative storm phase as yet in the European midlatitude sector. However, in addition to the disturbance dynamo, other contributions toward the presence of a negative ionospheric storm phase in the American sector may come from the equatorward movement of the midlatitude density trough and the equatorward compression of the plasmapause, which are discussed in the following section.

4.2. Midlatitude Density Trough and the Midlatitude Shoulder

The ionospheric midlatitude trough is a phenomenon observed near the equatorward edge of the auroral oval characterized by strong density depletions, generally extended from the post afternoon to dawn sector [*Kersley et al.*, 1997]. In general, it has three structures associated with it: an equatorward edge, a trough minimum, and a poleward edge [*Rodger et al.*, 1992]. The phenomenon is believed to be caused by the opposite nature of the horizontal plasma drift in the equatorward and the poleward portions of the ionosphere. In the equatorward portion of the dark region, the plasma drifts eastward, whereas in the poleward portion, the plasma drifts westward. This results in a narrow band of latitude where there is a strong depletion in plasma density leading to the formation of the midlatitude density trough [*Knudsen*, 1974; *Spiro et al.*, 1978; *Collis and Haggstrom*, 1988]. The position of the trough varies from longitude to longitude depending upon the alignment of the geomagnetic equator or, more importantly, the offset between the geographic and the geomagnetic equator. For example, using the Constellation Observing System for Meteorology, Ionosphere and Climate (COSMIC) electron density profiles, *He et al.* [2011] has shown that in the European sector, the trough can be observed above 60° of geographic latitude in both hemispheres during March equinox. However, in the American sector, the trough can be formed around slightly lower latitudes (50°–60°), in the Northern Hemisphere, during geomagnetically quiet conditions, during the same period. This shift is caused by the strong southward offset between the magnetic and geographic equators. However, the midlatitude trough is known to move equatorward during increased geomagnetic activity [*Spiro et al.*, 1978; *Pryse et al.*, 2006].

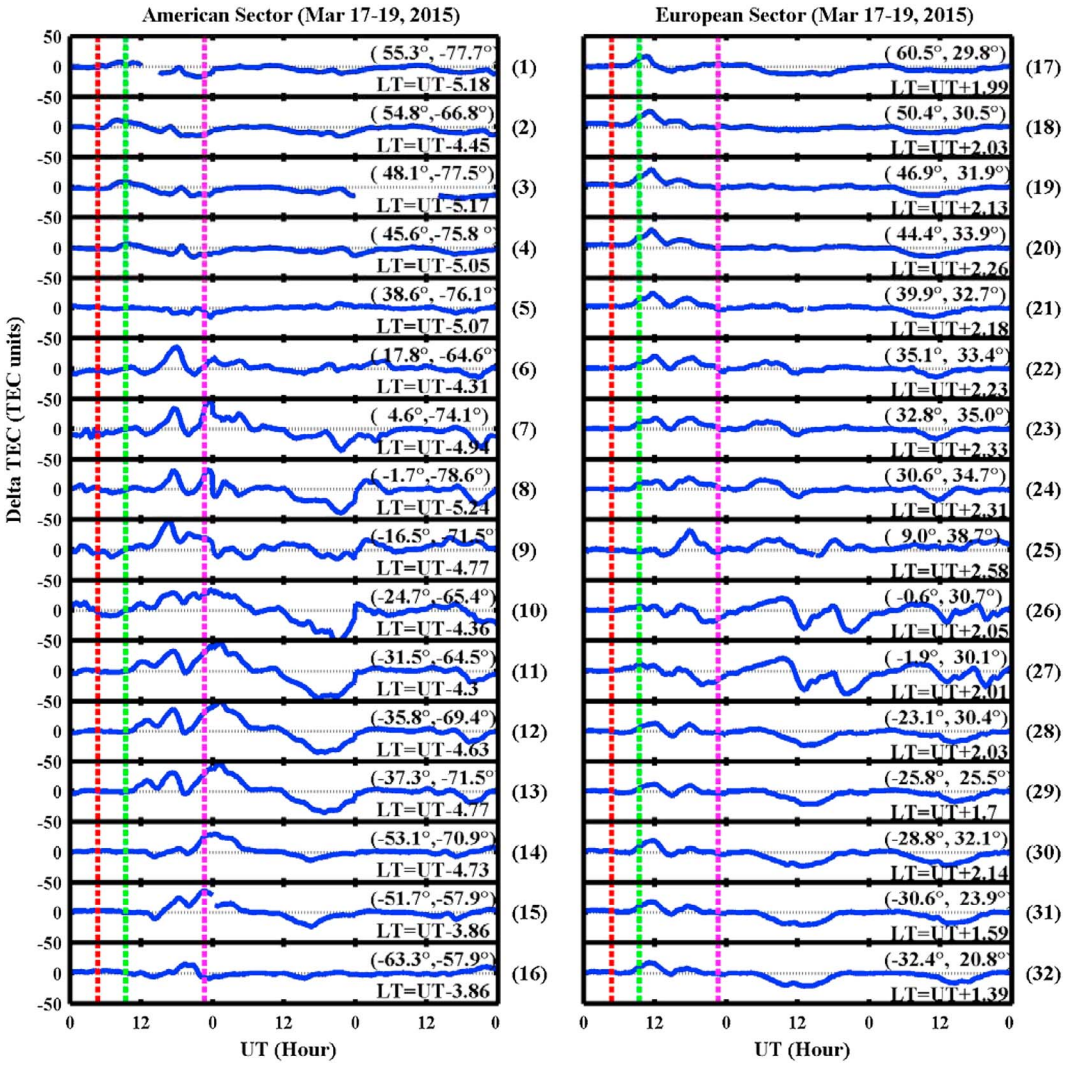

Figure 5. Variations of ΔTEC (storm time TEC − quiet time TEC). (rows 1–16) The variations of ΔTEC in the American sector and (rows 17–32) the variations in the European sector. The latitude and longitude of each station is mentioned in the top right corner, and the local time (LT) represented as a function of universal time (UT) is mentioned in the bottom right corner of each panel.

To prove the point further, let us have a look at Figure 6 which shows the in situ electron density measurement by SWARM A satellite at around 450 km. Here we consider two consecutive postsunset SWARM A passes above the American sector to verify the simultaneous presence of positive and negative storm phases. In the figure, the plots in blue, red, and green represent the SWARM A passes on 16–18 March, respectively. All these passes are in the postsunset sector, and the local time of each pass in the concerned longitude is close to 20 h LT. Figures 6a and 6d show the in situ electron density as a function of geographic latitude, Figures 6b and 6e represent the latitudinal-longitudinal extent of each pass, and Figures 6c and 6f plot the in situ electron densities of each pass as a function of universal time (UT). On the left-hand side (Figures 6a–6c), shown in red is a SWARM pass from 23:00 to 23:40 UT on 17 March 2015 which passes though −60° longitude. The 16 March pass shown in blue passing through a nearby longitude can be considered as a quiet time pattern in this case. First of all, the increase in peak electron density in the crest regions as well as the huge enhancement in the latitudinal extent of the equatorial ionization anomaly can be noticed on 17 March. This proves the presence of an eastward prompt penetration electric field (PPEF) leading up to the formation of this stronger anomaly which is also sometimes termed as the superfountain effect [*Tsurutani et al.*, 2008].

The second important thing to note is the sharp drop in electron density at latitudes of 40°N in the Northern Hemisphere and at around −60° in the Southern Hemisphere, accompanied by a v-shaped depletion just

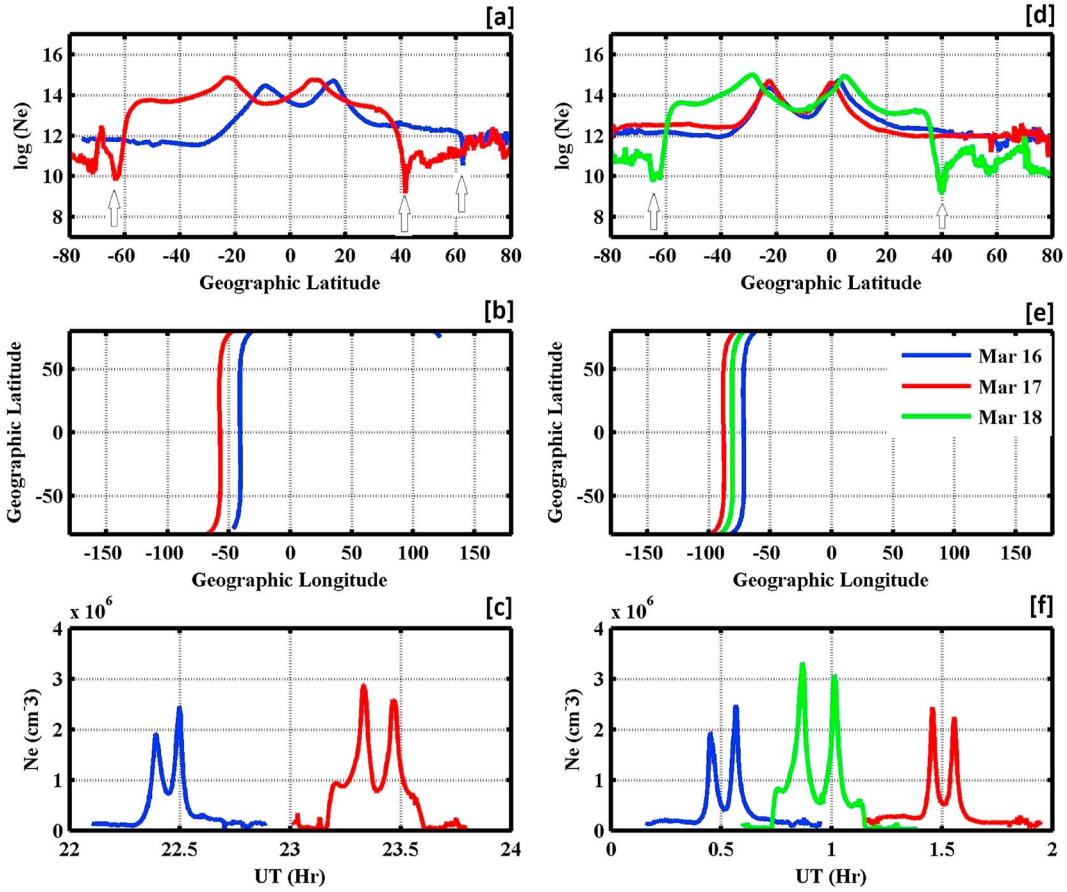

Figure 6. SWARM A passes over the American sector showing strong equatorward shift of the midlatitude density trough (marked by the arrows) in the Northern Hemisphere in the American sector. The trough minimum is observed reaching up to 40°N during the disturbed period. The quiet time passes do not show such equatorward shift.

poleward to it. This sharp drop in density at 40°N, also known as the "midlatitude shoulder," is the signature of the plasmapause. The "shoulder" is generally formed when the midlatitude/high-latitude plasma density is eroded due to the compression of the plasmapause under the action of the magnetospheric convection electric fields [*Tsurutani et al.*, 2004; *Horvath and Lovell*, 2008]. The v-shaped depletion immediately poleward of the shoulder represents the midlatitude density trough. In this case, the midlatitude density trough has moved equatorward till 40°N in the Northern Hemisphere under the geomagnetically disturbed conditions.

The next consecutive SWARM A pass from around 00:35 to 01:25 UT on 18 March 2015 is shown on the right-hand side (Figures 6d–6f). In this case the green curve represents the disturbed time pass about −80° longitude. The blue pass for 16 March represents the quiet time pattern as usual. At the same time, the red curve for 17 March also represents a quiet time pattern in this case as the time of the satellite pass (01:05–01:50 UT) is well before the onset of the geomagnetic storm. In agreement with Figure 6a, Figure 6d also shows a strong latitudinal enhancement of the EIA as shown in the green curve which overshadows the EIAs for the blue and red curves. Sharp depletions in densities are observed at around latitudes of 40° and −60°.

The same depletions are observed in ground-based ionograms as shown in Figures 3a and 3b for Boulder and Millstone Hill, respectively. In fact, in case of Millstone Hill (42.6°N), a complete fade-out in the ionograms is observed from 00:00 to 11:00 UT of 18 March 2015, when no reflected echoes were received. Such a fade-out can occur mainly due to two reasons: (i) decrease in *F* region electron density beyond the minimum capability of the diagnosed and (ii) *D* region absorption of the incident radio waves due to strong particle precipitation in the lower atmosphere. In our case, both may be the reasons. As shown in Figure 6, the ionospheric electron density was well below its normal values. At the same time, the severe depletion at 40°N can be inferred as an evidence of the equatorward movement of the midlatitude trough and an indirect evidence of the

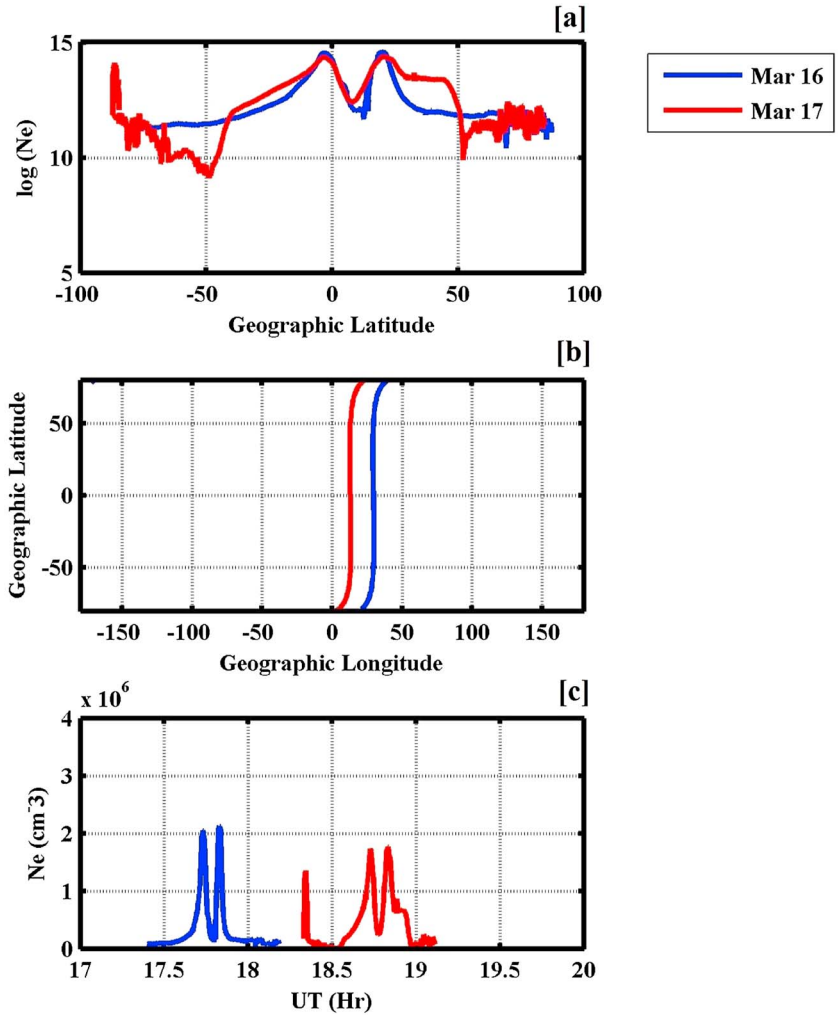

Figure 7. Midlatitude density trough as seen through SWARM A in the European sector.

equatorward expansion of the auroral oval in the Northern Hemisphere, in the American sector. The signature of auroral oval can be seen around 50°N as a small peak in density which is caused by auroral ionization. In the Southern Hemisphere, however, the depletion is seen at around −60° of latitude because the midlatitude trough and the shoulder are both located around that latitude region. However, the depletion in f_oF_2 seen at Eglin (Figure 3c) cannot be attributed to the midlatitude density trough since the location of Eglin (30.5°N) falls outside the boundary of the midlatitude trough.

Figure 7 shows a figure similar to Figure 6, for the European sector. The SWARM A pass in this case goes through 10°E longitude between 18:20 and 19:05 UT on 17 March 2015. The boundary marked by the depletion in electron density is situated at 50° latitudes in both hemispheres. Also, the depletion does not seem that strong as compared to that in the American sector. Also, the latitudinal extent of the EIA seems relatively lesser when compared to that of the American sector. However, it must be remembered that due to the South Atlantic Magnetic Anomaly, the EIA is mostly formed significantly stronger in the American longitude sector as compared to other longitudes [*Tsurutani et al.*, 2004, 2008]. This may be one of the reasons behind the relatively less dramatic effects observed in the European sector during and around the main phase of the storm when compared to the American sector.

So on the basis of the above evidences, it can be summarized that the enhanced negative storm phase observed in the American sector has multiple contributions from the equatorward movement of the midlatitude density trough, the compression of the plasmapause which is seen as the density shoulder, and possible presence of disturbance dynamo electric fields. *Lu et al.* [2001] was the first to report the coexistence

of positive and negative ionospheric storm phases. While investigating the 10 January 1997 geomagnetic storm, the authors observed a coexistence of both positive and negative storm phases in the Northern (winter) Hemisphere. The presence of both opposite phases were attributed to complex dynamical and chemical interactions between the charged particle and the neutral atmosphere during geomagnetic disturbances. However, in this case, the asymmetric meridional wind from summer to winter hemispheres is also considered to be a major driver. Keeping that in mind, the presence of both positive and negative storm phases during equinox is difficult to explain. Also, although the contribution of dynamically changing neutral atmosphere during a magnetically disturbed period is agreed upon, the contribution of the geomagnetic field structure in the American sector should also be looked into since the coexistent positive and negative storm phases are generally observed in this particular sector [*Horvath and Lovell*, 2015].

4.3. Negative Ionospheric Storm Phase During the Recovery Phase of the Storm

After 04 UT on 18 March, the IMF B_z almost recovers to its normal state (values near 0 nT) with relatively smaller fluctuations. After this period of time, the possibility of prompt penetration of electric field gradually decreases. At the same time, the disturbance dynamo electric fields start to take over the dynamics of the equatorial, low-latitude, and midlatitude ionosphere. The American sector (Figure 3) does not show much variation from its quiet time pattern. The European sector gets affected strongly. The h_mF_2 shows small increase from its normal quiet day pattern (Figures 4g–4l). On the contrary, the f_oF_2 (Figures 4a–4f) continues to be on the lower side as compared to its normal quiet time pattern which signifies a negative ionospheric storm which continues for 18 and 19 March as well. So for almost 48 h, the European sector ionosphere undergoes a negative ionospheric storm during the recovery phase of the geomagnetic storm, the effects being much more prominent on the Southern Hemisphere as compared to the northern one. In fact, for Athens station the decrease in f_oF_2 seems very negligible. It can be seen that for 18 and 19 March 2015, the stations in the Southern Hemisphere show a clear decrease in TEC in both sectors representing the negative ionospheric storm. For stations in the Northern Hemisphere, though there is decrease in TEC, it is not that noticeable as compared to that in the Southern Hemisphere.

The presence of such an asymmetry in hemispherical behavior is difficult to explain considering the fact that this storm (17–19 March) occurred during the equinox. In simple words, the hemispherical asymmetry is generally created due to the asymmetry in the thermospheric wind patterns in the two hemispheres. The winds become strongly asymmetric during solstices (summer/winter). On the other hand, during equinoxes, the winds become relatively less asymmetric. However, it would be wrong to say that the winds become exactly symmetric during equinoxes. Generally, during geomagnetic disturbances, the modified wind pattern gets superimposed on the background wind pattern which is generally from summer hemisphere to winter hemisphere [*Prölss*, 1995; *Fuller-Rowell et al.*, 1996; *Goncharenko et al.*, 2007].

To have a better idea of the thermospheric neutral density, we looked at the global daily maps of the thermospheric O/N_2 ratio produced using the Global Ultraviolet Imager (GUVI) instrument on board TIMED (Thermosphere Ionosphere Mesosphere Energetics and Dynamics) spacecraft. Figures 8a–8e represent the global O/N_2 ratio for 15–19 March 2015, respectively. The white oval patches in Figures 8a–8e represent the South Atlantic Anomaly region. In this region, the signal from atmospheric emission is contaminated due to enhanced radiation from particles from the Earth's radiation belt. So the data from that region is removed, which is represented by the white oval patch. As seen from Figure 8c, the O/N_2 ratio shows a sharp decrease in the American sector as compared to that on the quiet days of 15–16 March 2015 (Figures 8a and 8b). This decrease in O/N_2 ratio on 17 March also confirms the negative storm phase in the American sector as seen in f_oF_2 (Figure 3), GPS TEC (Figure 5), and the SWARM passes over the American sector (Figure 6). On 18 March (Figure 8d), the decrease in O/N_2 ratio seems to have reached regions more equatorward, particularly in the Southern Hemisphere as compared to the Northern Hemisphere. This may explain the strong negative storm phases observed in the Southern Hemisphere in both the American and European sectors, as seen in Figure 5. On 19 March, the O/N_2 ratio seems to slightly recover toward its normal quiet time values, although it still shows reduced values in the European sector. This explains the still existing negative storm phases on 19 March as seen in Figure 5.

In a recent study, *Astafyeva et al.* [2015] has also reported the strong negative ionospheric storm phase and the hemispheric asymmetry during the recovery phase of the 17–19 March 2015 storm. The authors have also tried to explain the hemispherical asymmetry in terms of the asymmetry in the Earth's geomagnetic field and the orientation of IMF B_y. It must be considered that IMF B_y plays a role in creating asymmetry during the

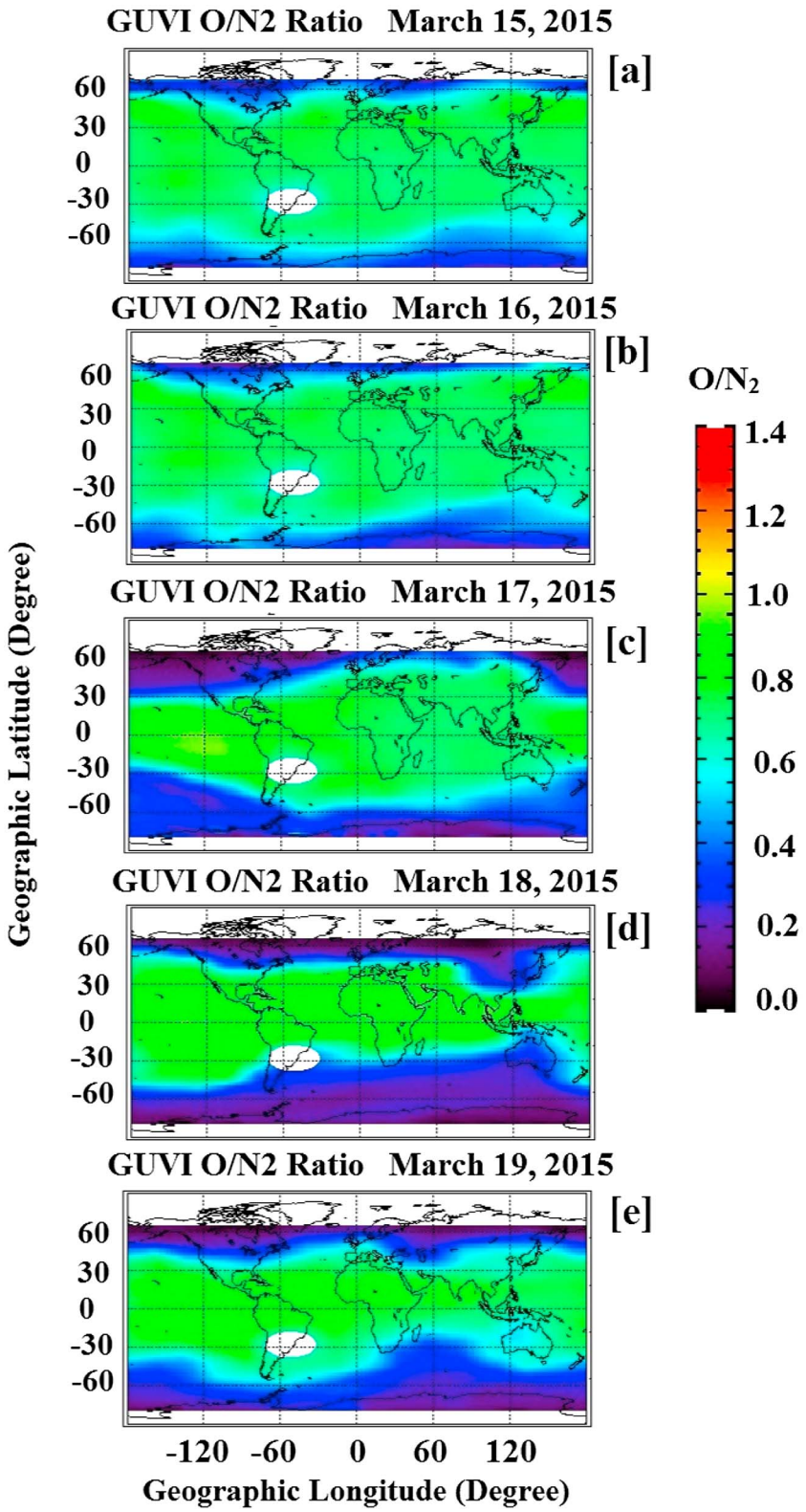

Figure 8. Thermospheric O/N_2 global maps produced from TIMED-GUVI for (a–e) 15–19 March 2015.

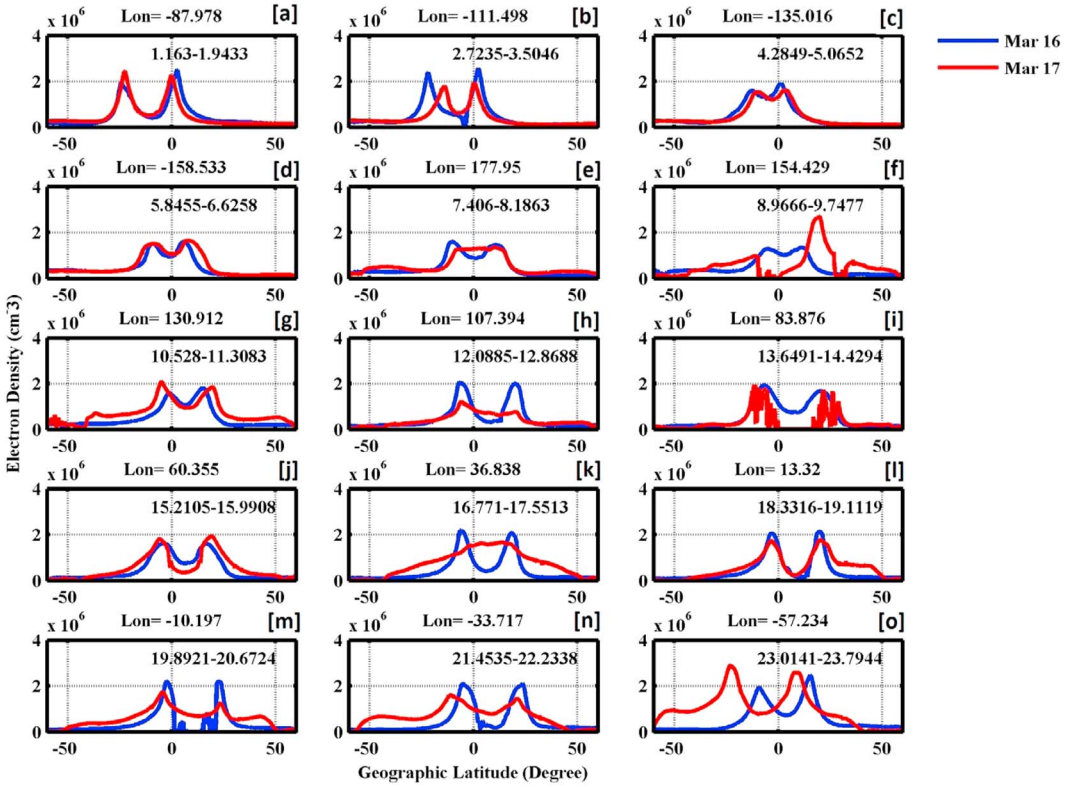

Figure 9. Evolution of EIA on 17 March 2015 across different longitudes.

storm time dynamics but particularly in the high latitudes [*Laundal and Østgaard*, 2009; *Crowley et al.*, 2006; *Förster et al.*, 2011]. The most important driver behind the negative storm phase is the compositional changes in the thermospheric neutral wind during a magnetically disturbed period [*Fuller-Rowell et al.*, 1997; *Prölss*, 1997; *Buonsanto*, 1999]. The main reason behind the asymmetry lies somewhere in the dynamics of meridional thermospheric wind. Unfortunately, not many measurements of the neutral wind are available right now. In future, with the availability of more wind measurements, such a question can be answered.

4.4. A Picture of EIA as Seen Through SWARM

As mentioned in section 2, all three satellites in the SWARM constellation are polar orbiting with the orbital inclination of each satellite being 87.5°. As a result, each single crossing of a satellite practically covers one longitudinal sector. So it gives us an excellent tool to look at the dynamics of the equatorial ionization anomaly (EIA). Figures 9a–9o and 10a–10o show the consecutive SWARM A passes on the postsunset side of the Earth for 17 and 18 March, respectively. The altitude of the satellite is approximately 450 km. In both figures, the blue curves represent the passes for 16 March which can be used as a quiet day pattern in this case. In Figure 9, the red curves represent the passes for 17 March. The equatorial crossing longitude of each pass is mentioned on the top of each panel, and the time duration of each pass is mentioned in UT in text, inside each panel. It should be noted that, for Figures 9a–9c, the period was still geomagnetically quiet. So the storm effects should be expected from Figures 9d–9o.

Figure 9e shows a peculiar EIA where there is no presence of any trough or crest. Instead, the density profile seems to be flat between the two crests indicating nearly similar densities between all the latitudes between the two crests. The next panel (Figure 9f) shows another interesting feature where we can see that the EIA is totally suppressed in the Southern Hemisphere, whereas in the Northern Hemisphere the EIA is formed very strongly. The peak density of the crest is almost double that of the normal quiet time crest density. The next two panels show opposing behaviors. On the one hand, Figure 9g shows the enhancement of EIA at around 130° of longitude, whereas Figure 9h shows the suppression of the EIA at around 107° of longitude.

The next panel shown in Figure 9i shows one of the most interesting features in this case. It should be noted that instead of a well-defined pattern, the red curve shows a highly fluctuating pattern. This represents the

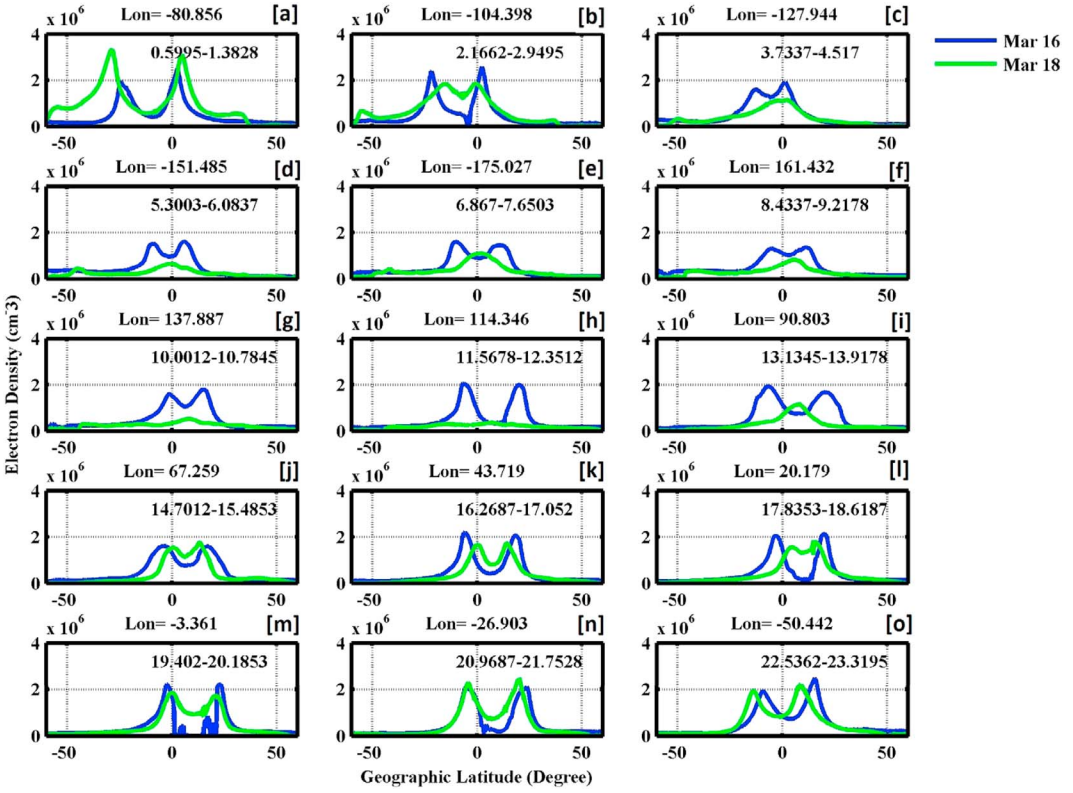

Figure 10. Evolution of EIA on 18 March 2015 across different longitudes.

presence of plasma bubbles formed at that longitude (Indian sector). The presence of plasma bubbles and the associated density depletions during a magnetic storm is not a new phenomenon. However, it should also be noted that near the trough region of the EIA, which also represents the geomagnetic equator, the density is found to be less than 1000/cm^3 which is way too less than its quiet time values. A similar feature is also seen in in the quiet time blue curve (16 March) in Figure 9m. Such a peculiar phenomenon is created due to the presence of a strong zonal eastward electric field which lifts the whole *F* layer ionosphere well above the altitude of the satellite pass (450 km in this case). Since the ionosphere itself is lifted well above its path, the satellite measures such a small density which seems much smaller than the quiet time values. Such a feature was first detected and explained by *Greenspan et al.* [1991] using DMSP satellite observations during 13–14 March 1989. The authors termed the phenomenon as "equatorial holes." The particular SWARM observation (Figure 9i) was also discussed in a recent study by *Ram et al.* [2015]. They also suggest the presence of a strong eastward prompt penetration electric field in the Indian longitudes which superposed on the prereversal enhancement (PRE) electric field to lift the equatorial plasma to higher altitudes and the corresponding enhancement of the EIA. The presence of PPEF was also reported by *Ramsingh et al.* [2015] in the Indian longitudes on 18 March. Using ground-based ionosonde data, the authors have shown a strong upliftment of the *F* region, postsunset. The authors have also reported the occurrence of F_3 layers on 18 March at the equatorial station Tirunelveli. It should be noted that the F_3 layer generally occurs during low solar activity period, whereas 2015 was still near the peak of solar cycle 24. The F_3 layer, which is a daytime phenomenon, generally forms during a time when the vertical $E \times B$ drift at equator is strong and fast increasing (instead of a steadily increasing $E \times B$ drift) [*Balan et al.*, 2000; *Nayak et al.*, 2014]. During magnetically disturbed periods, the formation of F_3 layer requires the presence of prompt penetration electric fields (PPEFs) [*Balan et al.*, 2008]. Hence, the presence of F_3 layer at Tirunelveli indirectly shows the presence of eastward PPEFs at the magnetic equator, in the Indian sector.

The EIA is seen to be formed nicely in Figures 9j–9o except for Figure 9k. Surprisingly, Figure 9k shows the EIA to be totally suppressed with a peak at the equator. This is quite similar to Figure 9e. This behavior may be due to possible presence of traveling ionospheric disturbances (TIDs). *Horvath and Lovell* [2010] have shown that the presence of TIDs can significantly affect the formation of EIA, at times destroying it.

Figures 10a–10o are actually more like a continuation of Figure 9 since it shows the consecutive passes in the postsunset sector for 18 March 2015. Figure 10a shows the EIA formation at a longitude of −80° in the American sector. Incidentally, this is the strongest formed EIA in terms of latitudinal extent with southern crest at 30°S and the northern crest at 5°N. Even at latitudes poleward of the crests, the ionization is remarkably higher than its quiet time values. Undoubtedly, this can be categorized as the superfountain effect as discussed by *Tsurutani et al.* [2008], which is caused by the intensification of the prereversal enhancement electric field (PRE) due to the additional presence of PPEFs and the effects of the South Atlantic magnetic anomaly (SAMA) which generally makes the EIA stronger in the American sector as compared to any other longitudinal sector [*Tsurutani et al.*, 2004, 2008].

After 02 UT on 18 March 2015, during the recovery phase of the storm, IMF B_z gradually reaches around values of 0 nT without much sudden fluctuations, as seen from Figure 2. Hence, the possibility of any strong PPEFs can be ruled out after this. However, there is a possibility of the disturbance dynamo electric fields reaching the equatorial latitudes by this time. This can be inferred from Figures 10b–10l where we can see a gradual suppression of the EIA accompanied by decrease in electron density as well. Such a scenario points toward the presence of a westward disturbance dynamo electric field. The westward electric field gives rise to a vertically downward $E \times B$. This vertically downward $E \times B$ drift pushes the plasma downward in altitude across the horizontal magnetic field lines giving rise to low plasma pressure region in the topside ionosphere. This gradually leads to the formation of the reverse plasma fountain where plasma flows toward the magnetic equator from the high-pressure crest regions to balance the low-pressure one [*Balan and Bailey*, 1995; *Horvath and Essex*, 2003]. This reverse plasma fountain, in turn, breaks and suppresses the EIA. Also, the lower altitudes result in enhanced recombination and corresponding loss of ionization. This is evident from Figures 10f–10h where the peak density at equator is much smaller than the normal quiet time values. After 14 UT, the EIA seems to get formed at different longitudes and gradually seems to attain its normal latitudinal extent as seen from Figures 10j–10o.

5. The Disturbed Ionosphere as Seen Through the IRTAM Global Maps

As discussed in section 2.3, the IRTAM has the potential to be used as a near-real-time tool to study the ionospheric variations during geomagnetically disturbed conditions. In this regard, we have looked at the global f_oF_2 maps for 17–18 March 2015. Figures 11a–11l show the global maps of Δf_oF_2 (IRTAM − IRI) of 4 h of resolution. The Δf_oF_2 maps are created by taking a difference of IRTAM f_oF_2 and the IRI model f_oF_2 values where the IRI is considered as a climatological model representing the geomagnetically quiet time conditions. Figures 11a–11c do not show much effects as the ionosphere is yet to be affected by the storm. The effects start showing up at 12:07 UT of 18 March 2015 (Figure 11d) where we can see clear intensification of the f_oF_2 values in the anomaly crest regions of the European sector. The same enhancement in f_oF_2 can also be seen in Figure 5. In the next three maps (Figures 11e–11g), we can see the appearance of density holes in the American sectors, which represent the strong negative storm phase during the main phase of the storm that we have discussed in sections 4.1 and 4.2. At the same time, we can see the enhancement in f_oF_2 near the equatorial regions indicating the possible presence of both positive and negative storm phases. Figures 11i–11l show the suppression of the EIA on 18 March 2015, under the presence of the westward disturbance dynamo, because of which we can see an enhancement in f_oF_2 in the equatorial regions. The SWARM A density profiles also gave a similar picture as discussed in section 4.4.

The IRTAM maps, however, do not clearly depict the negative storm phases on 18 March 2015 in the Southern Hemisphere which was discussed in section 4.3. Although Figures 11i–11j show the depletions in f_oF_2, Figures 11k and 11l fail to show the same depletions. Also, it fails to show the hemispheric asymmetry in this case. However, the IRTAM maps show another interesting feature. In Figure 11g, we can see a density hole (depletion in f_oF_2) appearing over the Chinese region at 00:07 UT of 18 March 2015. In the subsequent maps (11h–11k), the density hole can be seen evolving and moving toward the equator. This may represent the traveling ionospheric disturbances (TIDs). However, this is beyond the scope of this study. Overall, the IRTAM seems to perform quite well when compared to other independent measurements and it can be used as a tool to study the ionospheric space weather conditions because of its ability to work near real time.

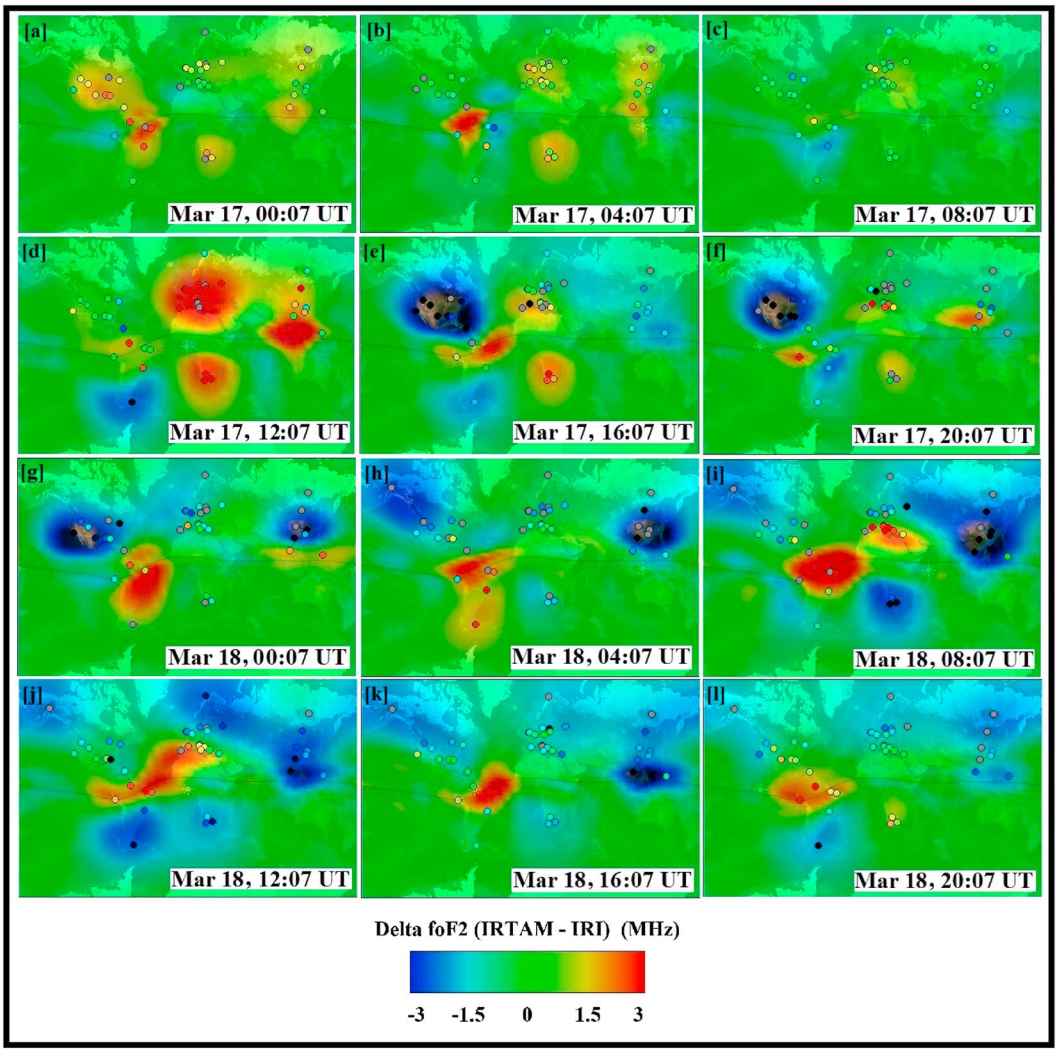

Figure 11. IRTAM $\Delta f_o F_2$ maps for 17–18 March 2015.

6. Conclusion

In the present paper, we have studied the effects of the 17–18 March 2015 geomagnetic storm on the low-latitude and midlatitude ionosphere in two different longitudinal sectors, using two chains of ground-based ionosondes and GPS TEC observations along with SWARM in situ density measurements. Our study has done a detailed analysis of the storm effects with the underlying physical mechanisms and tried to explain them on the basis of available evidences across two longitudinal sectors. Also, we have used the IRTAM for the first time as an ionospheric space weather tool. The major conclusions of the present study are listed below.

1. During the main phase of the storm, simultaneous presence of positive and negative ionospheric storm phases are observed in the American sector, whereas no such coexistent storm phases are observed in the European sector. For the American sector, the coexistent positive and negative ionospheric storm phases are seen in both hemispheres.
2. In the American sector, the midlatitude density trough is observed to shift equatorward reaching up to 40°N latitude. This equatorward shift of the midlatitude density trough, along with the compression of plasmapause and the presence of disturbance dynamo-related effects, plays a major role in the negative ionospheric storm phase observed in this sector during the main phase of the storm. The effects are much more enhanced due to the presence of the South Atlantic magnetic anomaly (SAMA). Although the negative

storm phases are present in the European sector during the main phase, they are less developed as compared to the American sector.

3. Strong hemispherical asymmetry is observed during the recovery phase of the storm in both longitudinal sectors. The ionospheric electron density shows sharp decrease in the Southern Hemisphere as seen in both ground-based ionosonde and GPS TEC observations. On the contrary, the Northern Hemisphere does not show such depletions in electron density.
4. The SWARM electron density measurements show the formation of the superfountain just after the maximum phase of the storm which proves the presence of eastward prompt penetration electric fields (PPEFs). However, afterward, the EIA is observed to be suppressed across all longitudes showing the presence of westward disturbance dynamo electric fields at the equator.
5. For the first time, we have utilized the IRI Real-Time Assimilative Mapping (IRTAM) as a tool to study the ionospheric space weather conditions. The IRTAM performs quite well in accordance with independent measurements and can be utilized in future as a powerful near-real-time tool to study the ionospheric variations during geomagnetically disturbed conditions.

Acknowledgments

The research is partially supported by the project "MOST 104-2111-M-008-013" of National Central University, Taiwan, granted by Ministry of Science and Technology, Taiwan. One of the authors, Punyawi Jamjareegulgarn, sincerely acknowledges the financial support from the annual government budget in A.D. 2016, Thailand. We thank the NASA/GSFCs Space Physics Data Facilitys OMNIWeb service for data of the interplanetary and *SYM-H* parameters. We also thank the Global Ionospheric Radio Observatory (GIRO) (http://giro.uml.edu/) for providing the ionosonde data and the IRTAM tool for this study. We are grateful to the Scripps Orbit and Permanent Array Center (SOPAC), (http://sopac.ucsd.edu/dataBrowser.shtml) for the GPS TEC data. We are thankful to the ESA EarthNet service for providing the SWARM data (http://earth.esa.int/SWARM). We also thank the Johns Hopkins University Applied Physics Laboratory (http://guvitimed.jhuapl.edu) for providing the thermospheric O/N_2 density maps from the TIMED-GUVI.

References

Astafyeva, E., Y. Yasyukevich, A. Maksikov, and I. Zhivetiev (2014), Geomagnetic storms, super-storms, and their impacts on GPS-based navigation systems, *Space Weather*, *12*, 508–525, doi:10.1002/2014SW001072.

Astafyeva, E., I. Zakharenkova, and M. Förster (2015), Ionospheric response to the 2015 St. Patrick's Day storm: A global multi-instrumental overview, *J. Geophys. Res. Space Physics*, *120*, 9023–9037, doi:10.1002/2015JA021629.

Balan, N., and G. J. Bailey (1995), Equatorial plasma fountain and its effects: Possibility of an additional layer, *J. Geophys. Res.*, *100*, 21,421–21,432, doi:10.1029/95JA01555.

Balan, N., I. S. Batista, M. A. Abdu, G. J. Bailey, S. Watanabe, J. MacDougall, and J. H. A. Sobral (2000), Variability of an additional layer in the equatorial ionosphere over Fortaleza, *J. Geophys. Res.*, *105*, 10,603–10,613, doi:10.1029/1999JA000020.

Balan, N., S. V. Thampi, K. Lynn, Y. Otsuka, H. Alleyne, S. Watanabe, M. A. Abdu, and B. G. Fejer (2008), F_3 layer during penetration electric field, *J. Geophys. Res.*, *113*, A00A07, doi:10.1029/2008JA013206.

Basu, S., K. M. Groves, H.-C. Yeh, S.-Y. Su, F. J. Rich, P. J. Sultan, and M. J. Keskinen (2001), Response of the equatorial ionosphere in the South Atlantic region to the great magnetic storm of July 15, 2000, *Geophys. Res. Lett.*, *28*, 3577–3580, doi:10.1029/2001GL013259.

Basu, S., S. Basu, J. J. Makela, E. MacKenzie, P. Doherty, J. W. Wright, F. Rich, M. J. Keskinen, R. E. Sheehan, and A. J. Coster (2008), Large magnetic storm-induced nighttime ionospheric flows at midlatitudes and their impacts on GPS-based navigation systems, *J. Geophys. Res.*, *113*, A00A06, doi:10.1029/2008JA013076.

Bhattacharyya, A., S. Basu, K. M. Groves, C. E. Valladares, and R. Sheehan (2002), Effect of magnetic activity on the dynamics of equatorial *F* region irregularities, *J. Geophys. Res.*, *107*(A12), 1489, doi:10.1029/2002JA009644.

Bilitza, D., L.-A. McKinnell, B. Reinisch, and T. Fuller-Rowell (2011), The international reference ionosphere today and in the future, *J. Geod.*, *85*, 909–920, doi:10.1007/s00190-010-0427-x.

Blanc, M., and A. D. Richmond (1980), The ionospheric disturbance dynamo, *J. Geophys. Res.*, *85*, 1669–1686, doi:10.1029/JA085iA04p01669.

Buonsanto, M. J. (1999), Ionospheric storms – A review, *Space Sci. Rev.*, *88*, 563–601, doi:10.1023/A:1005107532631.

Collis, P. N., and I. Haggstrom (1988), Plasma convection and auroral precipitation processes associated with the main ionospheric trough at high latitudes, *J. Atmos. Terr. Phys.*, *50*, 389–404, doi:10.1016/0021-9169(88)90024-4.

Crowley, G., et al. (2006), Global thermosphere-ionosphere response to onset of 20 November 2003 magnetic storm, *J. Geophys. Res.*, *111*, A10S18, doi:10.1029/2005JA011518.

Fejer, B. G., and L. Scherliess (1995), Time dependent response of equatorial ionospheric electric fields to magnetospheric disturbances, *Geophys. Res. Lett.*, *22*(7), 851–854, doi:10.1029/95GL00390.

Fejer, B. G., and L. Scherliess (1997), Empirical models of storm time equatorial zonal electric fields, *J. Geophys. Res.*, *102*, 24,047–24,056, doi:10.1029/97JA02164.

Förster, M., S. E. Haaland, and E. Doornbos (2011), Thermospheric vorticity at high geomagnetic latitudes from CHAMP data and its IMF dependence, *Ann. Geophys.*, *29*, 181–186, doi:10.5194/angeo-29-181-2011.

Foster, F. J., and J. C. Rich (1998), Prompt midlatitude electric field effects during severe geomagnetic storms, *J. Geophys. Res.*, *103*, 26,367–26,372, doi:10.1029/97JA03057.

Fuller-Rowell, T. J., M. V. Codrescu, H. Risbeth, R. J. Moffett, and S. Quegan (1996), On the seasonal response of the thermosphere and ionosphere to geomagnetic storms, *J. Geophys. Res.*, *101*, 2343–2354, doi:10.1029/95JA01614.

Fuller-Rowell, T. J., M. V. Codrescu, B. G. Fejer, W. Borer, F. Marcos, and D. N. Anderson (1997), Dynamics of the low-latitude thermosphere: Quiet and disturbed conditions, *J. Atmos. Terr. Phys.*, *59*, 1533–1540, doi:10.1016/S1364-6826(96)00154-X.

Galkin, I. A., B. W. Reinisch, X. Huang, and D. Bilitza (2012), Assimilation of GIRO data into a real-time IRI, *Radio Sci.*, *47*, RS0L07, doi:10.1029/2011RS004952.

Goncharenko, L. P., J. C. Foster, A. J. Coster, C. Huang, N. Aponte, and L. J. Paxton (2007), Observations of a positive storm phase on September 10, 2005, *J. Atmos. Sol. Terr. Phys.*, *69*, 1253–1272, doi:10.1016/j.jastp.2006.09.011.

Greenspan, M. E., C. E. Rasmussen, W. J. Burke, and M. A. Abdu (1991), Equatorial density depletions observed at 840 km during the great magnetic storm of March 1989, *J. Geophys. Res.*, *96*, 13,931–13,942, doi:10.1029/91JA01264.

He, M., L. Liu, W. Wan, and B. Zhao (2011), A study on the nighttime midlatitude ionospheric trough, *J. Geophys. Res.*, *116*, A05315, doi:10.1029/2010JA016252.

Heelis, R. A., J. J. Sojka, M. David, and R. W. Schunk (2009), Storm time density enhancements in the middle-latitude dayside ionosphere, *J. Geophys. Res.*, *114*, A03315, doi:10.1029/2008JA013690.

Horvath, I., and E. A. Essex (2003), Vertical $E \times B$ drift velocity variations and associated low-latitude ionospheric irregularities investigated with the TOPEX and GPS satellite data, *Ann. Geophys.*, *21*(4), 1017–1030, doi:10.5194/angeo-21-1017-2003.

Horvath, I., and B. C. Lovell (2008), Formation and evolution of the ionospheric plasma density shoulder and its relationship to the superfountain effects investigated during the 6 November 2001 great storm, *J. Geophys. Res.*, *113*, A12315, doi:10.1029/2008JA013153.

Horvath, I., and B. C. Lovell (2010), Large-scale traveling ionospheric disturbances impacting equatorial ionization anomaly development in the local morning hours of the Halloween superstorms on 29–30 October 2003, *J. Geophys. Res.*, *115*, A04302, doi:10.1029/2009JA014922.

Horvath, I., and B. C. Lovell (2015), Positive and negative ionospheric storms occurring during the 15 May 2005 geomagnetic superstorm, *J. Geophys. Res. Space Physics*, *120*, 7822–7837, doi:10.1002/2015JA021206.

Jakowski, N., V. Wilken, S. Schlueter, S. M. Stankov, and S. Heise (2005), Ionospheric space weather effects monitored by simultaneous ground and space based GNSS signals, *J. Atmos. Sol. Terr. Phys.*, *67*, 1074–1084, doi:10.1016/j.jastp.2005.02.023.

Kakad, B., K. Jeeva, K. U. Nair, and A. Bhattacharyya (2007), Magnetic activity linked generation of nighttime equatorial spread *F* irregularities, *J. Geophys. Res.*, *112*, A07311, doi:10.1029/2006JA012021.

Kelley, M. C., J. J. Makela, J. L. Chau, and M. J. Nicolls (2003), Penetration of the solar wind electric field into the magnetosphere/ionosphere system, *Geophys. Res. Lett.*, *30*, 1158, doi:10.1029/2002GL016321.

Kersley, L., S. E. Pryse, I. K. Walker, J. A. T. Heaton, C. N. Mitchell, M. J. Williams, and C. A. Willson (1997), Imaging of electron density troughs by tomographic techniques, *Radio Sci.*, *32*, 1607–1621, doi:10.1029/97RS00310.

Khmyrov, G. M., I. A. Galkin, A. V. Kozlov, B. W. Reinisch, J. McElroy, and C. Dozois (2007), Exploring digisonde ionogram data with SAO-X and DIDBase, *AIP Conf. Proc.*, *974*, 175–185, doi:10.1063/1.2885027.

Kikuchi, T., T. Araki, H. Maeda, and K. Maekawa (1978), Transmission of polar electric fields to the equator, *Nature*, *273*, 650–651, doi:10.1038/273650a0.

Kikuchi, T., H. Lühr, T. Kitamura, O. Saka, and K. Schlegel (1996), Direct penetration of the polar electric field to the equator during a *DP* 2 event as detected by the auroral and equatorial magnetometer chains and the EISCAT radar, *J. Geophys. Res.*, *101*, 17,161–17,174, doi:10.1029/96JA01299.

Kikuchi, T., H. Lühr, K. Schlegel, H. Tachihara, M. Shinohara, and T.-I. Kitamura (2000), Penetration of auroral electric fields to the equator during a substorm, *J. Geophys. Res.*, *105*, 23,251–23,262, doi:10.1029/2000JA900016.

Kikuchi, T., K. K. Hashimoto, and K. Nozaki (2008), Penetration of magnetospheric electric fields to the equator during a geomagnetic storm, *J. Geophys. Res.*, *113*, A06214, doi:10.1029/2007JA012628.

Knudsen, W. C. (1974), Magnetospheric convection and the high-latitude F_2 ionosphere, *J. Geophys. Res.*, *79*, 1046–1055, doi:10.1029/JA079i007p01046.

Laundal, K. M., and N. Østgaard (2009), Asymmetric auroral intensities in the Earth's Northern and Southern Hemispheres, *Nature*, *460*, 491–493, doi:10.1038/nature08154.

Liu, J., W. Wang, A. Burns, X. Yue, S. Zhang, Y. Zhang, and C. Huang (2016), Profiles of ionospheric storm-enhanced density during the 17 March 2015 great storm, *J. Geophys. Res. Space Physics*, *121*(1), 727–744, doi:10.1002/2015JA021832.

Liu, L., Y. Chen, H. Le, V. I. Kurkin, N. M. Polekh, and C.-C. Lee (2011), The ionosphere under extremely prolonged low solar activity, *J. Geophys. Res.*, *116*, A04320, doi:10.1029/2010JA016296.

Liu, L., J. Yang, H. Le, Y. Chen, W. Wan, and C.-C. Lee (2012), Comparative study of the equatorial ionosphere over Jicamarca during recent two solar minima, *J. Geophys. Res.*, *117*, A01315, doi:10.1029/2011JA017215.

Lu, G., A. D. Richmond, R. G. Roble, and B. A. Emery (2001), Coexistence of ionospheric positive and negative storm phases under northern winter conditions: A case study, *J. Geophys. Res.*, *106*(A11), 24,493–24,504, doi:10.1029/2001JA000003.

Maruyama, N., A. D. Richmond, T. J. Fuller-Rowell, M. V. Codrescu, S. Sazykin, F. R. Toffoletto, R. W. Spiro, and G. H. Millward (2005), Interaction between direct penetration and disturbance dynamo electric fields in the storm-time equatorial ionosphere, *Geophys. Res. Lett.*, *32*, L17105, doi:10.1029/2005GL023763.

Nayak, C. K., V. Yadav, B. Kakad, S. Sripathi, K. Emperumal, T. K. Pant, A. Bhattacharyya, and S. Jin (2014), Peculiar features of ionospheric F_3 layer during prolonged solar minimum (2007–2009), *J. Geophys. Res. Space Physics*, *119*, 8685–8697, doi:10.1002/2014JA020135.

Nishida, A. (1968), Geomagnetic DP 2 fluctuations and associated magnetospheric phenomena, *J. Geophys. Res.*, *73*, 1795–1803, doi:10.1029/JA073i005p01795.

Pavlov, A. V. (1994), The role of vibrationally excited nitrogen in the formation of the mid-latitude negative ionospheric storms, *Ann. Geophys.*, *12*(6), 554–564, doi:10.1007/s00585-994-0554-x.

Proelss, G. W. (1987), Storm-induced changes in the thermospheric composition at middle latitudes, *Planet. Space Sci.*, *35*, 807–811, doi:10.1016/0032-0633(87)90041-9.

Prölss, G. (1995), Ionospheric *F*-region storms, in *Handbook of Atmospheric Electrodynamics II*, pp. 195–248, CRC Press, Boca Raton, Fla.

Prölss, G. W. (1993), Common origin of positive ionospheric storms at middle latitudes and the geomagnetic activity effect at low latitudes, *J. Geophys. Res.*, *98*, 5981–5991, doi:10.1029/92JA02777.

Prölss, G. W. (1997), Magnetic storm associated perturbations of the upper atmosphere, *Geophys. Monogr. Ser.*, *98*, 227–241, doi:10.1029/GM098p0227.

Prölss, G. W., L. H. Brace, H. G. Mayr, G. R. Carignan, and T. L. Killeen (1991), Ionospheric storm effects at subauroral latitudes – A case study, *J. Geophys. Res.*, *96*, 1275–1288, doi:10.1029/90JA02326.

Prolss, M. J. (1978), Travelling atmospheric disturbances as a possible explanation for daytime positive storm effects of moderate duration at middle latitudes, *J. Atmos. Terr. Phys.*, *40*, 1351–1354, doi:10.1016/0021-9169(78)90088-0.

Pryse, S. E., L. Kersley, D. Malan, and G. J. Bishop (2006), Parameterization of the main ionospheric trough in the European sector, *Radio Sci.*, *41*, RS5S14, doi:10.1029/2005RS003364.

Ram, S. T., et al. (2015), Duskside enhancement of equatorial zonal electric field response to convection electric fields during the St. Patrick's Day storm on 17 March 2015, *J. Geophys. Res. Space Physics*, *121*, 538–548, doi:10.1002/2015JA021932.

Ramsingh, S. S., S. Sreekumar, S. Banola, K. Emperumal, P. Tiwari, and B. S. Kumar (2015), Low-latitude ionosphere response to super geomagnetic storm of 17/18 March 2015: Results from a chain of ground-based observations over Indian sector, *J. Geophys. Res. Space Physics*, *120*, 10,864–10,882, doi:10.1002/2015JA021509.

Reddy, A. (1992), Magnetospheric substorms and nighttime height changes of the F_2 region at middle and low latitudes, *J. Geophys. Res.*, *97*, 3039–3061, doi:10.1029/91JA01512.

Reinisch, B. W., and I. A. Galkin (2011), Global ionospheric radio observatory (GIRO), *Earth Planets Space*, *63*, 377–381, doi:10.5047/eps.2011.03.001.

Richards, P. G., and P. J. Wilkinson (1998), The ionosphere and thermosphere at southern midlatitudes during the November 1993 ionospheric storm: A comparison of measurement and modeling, *J. Geophys. Res.*, *103*, 9373–9390, doi:10.1029/98JA00289.

Rodger, A. S., R. J. Moffett, and S. Quegan (1992), The role of ion drift in the formation of ionisation troughs in the mid- and high-latitude ionosphere – A review, *J. Atmos. Sol. Terr. Phys.*, *54*, 1–30, doi:10.1016/0021-9169(92)90082-V.

Sastri, J. H., N. S. V. V. Jyoti, H. Chandra, and C. V. Devasia (2000), Ionospheric storm of early November 1993 in the Indian equatorial region, *J. Geophys. Res.*, *105*, 18,443–18,455, doi:10.1029/1999JA000372.

Solomon, S., L. Qian, and B. Alan (2013), The anomalous ionosphere between solar cycles 23 and 24, *J. Geophys. Res.*, *118*, 6524–6535, doi:10.1002/jgra.50561.

Spiro, R. W., R. A. Heelis, and W. B. Hanson (1978), Ion convection and the formation of the mid-latitude *F* region ionization trough, *J. Geophys. Res.*, *83*, 4255–4264, doi:10.1029/JA083iA09p04255.

Spiro, R. W., R. A. Wolf, and B. G. Fejer (1988), Penetrating of high-latitude-electric-field effects to low latitudes during sundial 1984, *Ann. Geophys.*, *6*, 39–49.

Tsurutani, B., et al. (2004), Global dayside ionospheric uplift and enhancement associated with interplanetary electric fields, *J. Geophys. Res.*, *109*, doi:10.1029/2003JA010342.

Tsurutani, B. T., et al. (2008), Prompt penetration electric fields (PPEFS) and their ionospheric effects during the great magnetic storm of 30–31 October 2003, *J. Geophys. Res.*, *113*, doi:10.1029/2007JA012879.

Vlasov, M., M. C. Kelley, and H. Kil (2003), Analysis of ground-based and satellite observations of *F*-region behavior during the great magnetic storm of July 15, 2000, *J. Atmos. Terr. Phys.*, *65*, 1223–1234, doi:10.1016/j.jastp.2003.08.012.

Yeh, H.-C., J. C. Foster, F. J. Rich, and W. Swider (1991), Storm time electric field penetration observed at mid-latitude, *J. Geophys. Res.*, *96*, 5707–5721, doi:10.1029/90JA02751.